ELSEVIER

Cryogenics 40 (2000) 779–788

Cryogenics

www.elsevier.com/locate/cryogenics

A parametric study on the cooling characteristics of an infrared detector cryochamber ☆

Ho-Young Kim *, Byung Ha Kang, Dae-Young Lee

Thermal/Flow Control Research Center, Korea Institute of Science and Technology, 39-1 Hawolgok-Dong, Sungbook-Gu, Seoul 136-791, South Korea

Received 27 November 2000; accepted 26 January 2001

Abstract

This work investigates the steady and transient cooling characteristics of an infrared (IR) detector cryochamber, which has a critical effect on the cooling load that a refrigeration system should carry away. The current thermal modeling considers the conduction heat transfer through a cold well, the gaseous conduction due to outgassing, and the radiation heat transfer. The steady cooling load is obtained by using a fin equation. The transient cooling performance, i.e., the cool-down time, is determined using a finite difference method. It is shown that the gaseous conduction plays an important role in determining the steady cooling load, whereas it has a negligible effect on the cool-down time due to a short thermal penetration depth. The steady cooling load increases linearly with the bore conductivity when it is high. However, when the bore conductivity is low and the gas pressure is high, the cooling load becomes more sensitive to the bore conductivity. The steady cooling load increases linearly with the difference between the ambient temperature and the detector operation temperature, but rather the cool-down time is proportional to the square of the temperature difference. The results of this work can be used to determine the thermally optimal design and operation conditions of the cryochamber.

Keywords: Cryochamber; Cooling load; Cool-down time

1. Introduction

Infrared (IR) detectors are widely used for such applications as temperature measurement, intruder and fire detection, robotics and industrial equipment, thermoelastic stress analysis, medical diagnostics, and chemical analysis. Among IR detector types, quantum detectors are employed for most thermal-imaging and range-finding systems [1,2]. Quantum detectors commonly need to be refrigerated below 80 K, and thus a cooling system should be equipped together with the detector system [3]. The cooling load, which should be removed by the cooling system to maintain the nominal operating temperature of the detector, critically depends on the insulation efficiency of the cryochamber housing the detector. Therefore, understanding the thermal phenomena arising in the cryochamber is of great importance.

In a cryochamber, conduction and radiation occur simultaneously and both the steady and transient responses are important. Due to these seemingly complicated heat transfer processes, no modeling efforts to understand the phenomena seem to exist to date. In this work, by modeling these heat transfer processes, we study the effects of various parameters on the cooling performance, both steady and transient, of a cryochamber. The results of this work can be used to determine the thermally optimal design and operation conditions of a cryochamber.

We analyze the heat transfer characteristics of a chamber whose configuration is as shown in Fig. 1, which is typically used in practice. Basically, the cryochamber consists of a vacuum vessel (outer cylinder), a cold well (inner axisymmetric thin-walled structure), and a feedthrough unit. The space between the vacuum vessel and the cold well is vacuumed to minimize heat leakage through gas. The IR detector is located on top of the cold well, which receives optical signal through an

☆ This paper was presented at the "Korea–Japan Joint Workshop on Applied Superconductivity and Cryogenics", Cheju-Do, Korea, October 2–4, 2000.

* Corresponding author. Tel.: +82-2-958-6709; fax: +82-2-958-5689.

E-mail address: hoyoung@kist.re.kr (H.-Y. Kim).

0011-2275/01/$ - see front matter
PII: S0011-2275(01)00033-9

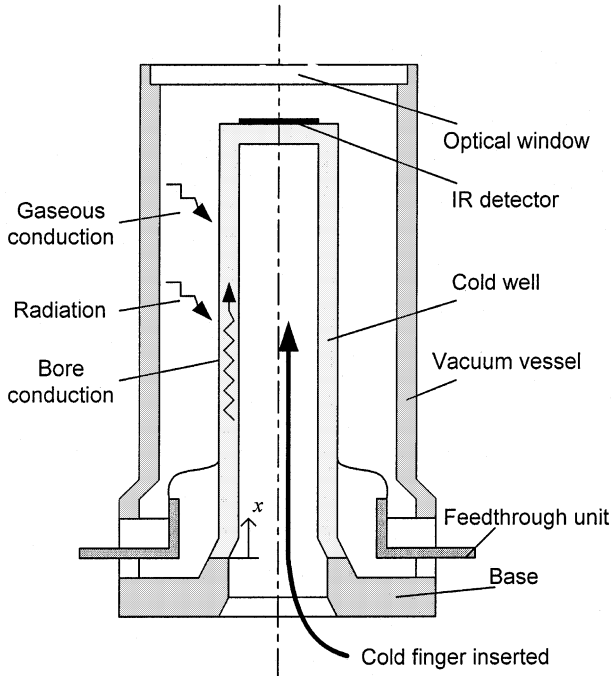

Fig. 1. A schematic diagram of a typical cryochamber and the mechanisms of heat transfer arising there.

IR window, i.e., the ceiling of the outer cylinder. The cold well shape can vary from cylindrical to conical and it houses a cold finger that removes heat from the detector. The cooling is executed by an external cryocooler, whose refrigeration schemes include Stirling, Joule–Thomson, Gifford–Mcmahon, and Vuilleumier cycles [4,5]. The feedthrough unit transmits the electronic signal from the detector to the exterior circuitry. It is typically placed at the base of the assembly as shown in the figure, but alternatively, it can be located at the level of the detector. In the former case, the cold well surface is electroplated with gold and is pattern-etched to conduct electronic signal from the detector down to the feedthrough unit. In the latter case, the direct gold wire bonding is used between the detector and the feedthrough unit. Table 1 summarizes the important elements in the assembly with their materials typically used. The dimensions and the physical properties of the elements used in this work are also listed in Table 1.

2. Thermal modeling

2.1. Steady heat transfer

Now we consider heat transfer paths along which heat from the outer environment is transmitted to the coldest region (cold tip) of the cryochamber. As shown in Fig. 1, heat is conducted from the base to the top of the cold well along a thin wall. In addition, radiative heat transfer occurs between the inner surface of the vacuum vessel and the outer surface of the cold well. Although the interior space between the cold well and the outer vessel is vacuumed, the remaining gas can participate in heat transfer depending on its pressure. However, natural convection hardly occurs in the configuration currently investigated due to its small dimensions. Assuming the annular interior space as a vertical large-aspect ratio enclosure, the Nusselt number based on the gap spacing is calculated to be nearly 1 [6], proving that the natural convection is negligible.

Since the cold well is made of very thin glass, whose thickness is of the order of 1 mm, the conduction can be assumed to be one-dimensional along the axial direction. That is, the Biot number defined as $Bi = hl_t/2k$, with h being the heat transfer coefficient for heat flow on the cold well surface, l_t the thickness of the cold well, and k the thermal conductivity of the cold well (glass bore), is much smaller than unity (at most 0.03 in the parameter range of this work). Therefore, the transverse thermal gradient is negligible compared to the axial thermal gradient. A detailed description on h is presented later in this section. We also assume that the cold finger inserted into the bore has the same temperature distribution as the cold well, thus neglect the heat transfer at the inside surface of the cold well.

In a steady state where the detector temperature is maintained at its nominal operating point (77 K), we have the following fin equation for a temperature distribution along the cold well [7]:

$$\frac{d^2\theta}{dx^2} - m^2\theta = 0, \tag{1}$$

where θ is the difference between the cold well temperature T and the temperature where the cold well faces

Table 1
List of elements constituting the cryochamber which are important in the thermal modeling

Element	Material	Dimensions	Properties
Vacuum vessel	Stainless steel	Inner diameter = 25 mm	$\varepsilon \approx 1$
Cold well	Borosilicate glass (outer surface is electroplated with gold)	Outer diameter = 9 mm Thickness = 1 mm Length = 48 mm	$\varepsilon = 0.02$ $\rho = 2640$ kg/m^3 $c = 800$ J/kg/K $k = 0.8$ W/m/K
Base	Stainless steel	–	–

the base, T_b, i.e., $\theta = T - T_b$, and x is as shown in Fig. 1. In addition, m^2 is given by $m^2 = \pi d_b h/kA_c$, where d_b and A_c are the outer diameter and the cross-sectional area of the cold well, respectively.

We neglect the thermal contact resistance between the metal (stainless steel) base and the glass bore since the glass is typically fused to be bond to the base. Therefore, T_b is the same as the temperature of the metal base, which is identical to the ambient temperature T_∞. On the other end of the glass bore, the detector array is bonded by epoxy. The detector array and its substrate is typically very thin, thus the detector is essentially at the same temperature as the top of the glass bore. Hence the temperature at both ends of the glass bore is specified, providing the boundary conditions to solve Eq. (1).

Solving Eq. (1) and substituting the foregoing boundary conditions, we obtain

$$T = T_\infty - (T_\infty - T_d)\frac{\sinh mx}{\sinh mL}, \tag{2}$$

where T_d is the detector temperature (77 K) and L the length of the cold well. The steady cooling load, Q_L, is determined by summing the conductive heat flux at the tip ($x = L$) and a heat generation in the detector when biased:

$$Q_L = -kA_c m(T_d - T_\infty)\frac{\cosh mL}{\sinh mL} + Q_{bias}. \tag{3}$$

It is now noted that the value of h is required to evaluate m. The heat transfer to the cold well surface consists of gaseous conduction and radiation from the vacuum vessel wall. Hence h is written as $h = h_{gc} + h_{rad}$, where h_{gc} is the thermal conductance of the gaseous conduction and h_{rad} the radiative heat transfer coefficient.

It is desired that the interior space be entirely vacuumed to prevent the gas occupying the space from participating in the heat transfer. Therefore, a getter is commonly used to get rid of residual gas molecules. However, as the detector is operated (the getter is off during detector operation), gas molecules that were bound to the surfaces are liberated, which phenomenon is called outgassing [8]. Due to outgassing, the interior gas pressure increases, and the contribution of the gaseous conduction to heat leakage increases. In spite of outgassing, the gas pressure usually stays below a limit to which the continuum hypothesis holds. Therefore, we need to consider the heat transfer in a rarefied gas, and its detailed discussion is presented in Appendix A. The theory states that there exist three regimes in the thermal conductance of the gaseous conduction depending on the gas pressure, as given by Eqs. (A.10)–(A.12) appearing in Appendix A.

Radiative heat transfer takes place between the cold well surface and the inner surface of the vacuum vessel. Assuming diffuse gray surface, the radiative heat flux between surfaces 1 and 2, Q_{rad}, is given by

$$Q_{rad} = \frac{\sigma(T_1^4 - T_2^4)}{R_{rad}}, \tag{4}$$

where σ is the Stefan–Boltzmann constant, and R_{rad} is written as [6]

$$R_{rad} = \frac{1-\varepsilon_1}{\varepsilon_1 A_1} + \frac{1}{A_2 F_{21}} + \frac{1-\varepsilon_2}{\varepsilon_2 A_2}. \tag{5}$$

Here ε is the emissivity and A the surface area. The subscripts, 1 and 2, correspond to the vacuum vessel wall surface and the outer surface of the cold well, respectively. T_1 is assumed to be the same as T_∞ owing to the effective insulation by high vacuum. F_{21} is the shape factor defined as the fraction of energy leaving A_2 that is intercepted by A_1. In our case, the emissivity of the vacuum vessel wall surface is close to 1, and the shape factor F_{21} is nearly unity as the geometry of Fig. 1 suggests. Therefore, the radiative heat flux that an infinitesimal area dA_2 of the cold well surface receives from the surface 1 can be written as

$$dQ_{rad} = \sigma\varepsilon_2\, dA_2(T_\infty^4 - T^4). \tag{6}$$

Now we make a further approximation that $T_\infty^4 - T^4 \approx 4T_m^3(T_\infty - T)$, where T_m is usually taken to be the mean of the surface temperatures when they are not too different. However, in our case, T_∞ is almost four times greater than T_L, the lowest value of T, thus taking a mere average temperature as T_m is not sufficiently accurate. Therefore, we seek a temperature that minimizes a functional F:

$$F = \left| \int_{T_d}^{T_\infty} [(T_\infty^4 - T_d^4) - 4T_m^3(T_\infty - T)]\, dT \right|, \tag{7}$$

which measures the difference in the total radiative heat fluxes computed by exact and approximate methods when the temperature distribution is linear with the location. It is found that $T_m = 237$ K results in $F = 0$. By utilizing this temperature, the radiation heat transfer coefficient is written as $h_{rad} = 4\varepsilon_2\sigma T_m^3 \approx 3\varepsilon_2$ [W/m^2 K]. Strictly speaking, this value yields an exact total radiation heat flux when the temperature distribution is linear with x. However, when the temperature distribution is not far from linear, this still provides a good approximation.

Using h_{gc} and h_{rad} obtained as above, we can calculate the steady cooling load from Eq. (3). We provide the calculation results obtained while varying parameters such as gas pressure, bore conductivity, and emissivity in Section 3.1.

2.2. Transient heat transfer

In addition to the steady cooling load, the transient thermal response of the detector is important since it is often required that the detector should be ready to work

within a short time, especially in military applications. The time it takes for the detector temperature to reach 77 K from T_∞ is referred to as the cool-down time, which is a primary measure of the transient performance of the detector cooling system. The energy balance in the cold well, considering one-dimensional unsteady conduction and surface heat flux, gives the following governing equation:

$$\frac{\partial T}{\partial t} = \alpha \frac{\partial^2 T}{\partial x^2} - \frac{m^2}{\rho c}(T - T_\infty), \tag{8}$$

where t is time, α, ρ, and c the thermal diffusivity, the density, and the thermal capacity of the glass bore, respectively. We consider a case where the cold well and the detector are initially at T_∞, and begin to cool as the cooler starts to operate at the cold tip. The base temperature remains constant at T_∞ throughout the time. Therefore, we obtain the following initial condition at $t = 0$ and a boundary condition at $x = 0$:

$$T = T_\infty \quad \text{at } t = 0, \tag{9}$$

$$T = T_\infty \quad \text{at } x = 0 \text{ for all } t. \tag{10}$$

The boundary condition at the other end is rather complicated since it is necessary to consider the thermal capacity of the top portion of the cold well as well as the side wall. Furthermore, the refrigeration capacity of a practical cooler is a function of its cold end's temperature, thus the heat removal rate at the cold tip depends on the cold tip's temperature. The data of the refrigeration capacity vs. the cold end's temperature can only be obtained empirically and differ in each cooler model. However, the refrigeration capacity of a cryocooler is roughly estimated as a linear function of the cold end's temperature in this work, based on the typical data shown in [4]. Therefore, the transient cooling rate, Q_c, is modeled as

$$Q_c = aT(t, x = L) + b \tag{11}$$

where a and b are specific to each cryocooler model. In this work, we used $a = 0.039$ W/K and $b = -2$ W. This is based on the performance of a cryocooler which has an input power of 35 W and a cooling capacity of 1 W at 77 K with 8.3% of the coefficient of performance relative to Carnot's at this temperature. To deduce the linear form of the refrigeration capacity with the temperature, we use another data point obtained by assuming the same % Carnot efficiency at 200 K ($Q_c = 5.8$ W). Then the coefficients a and b are obtained using the two data points at 77 and 200 K. We assume that Eq. (11) holds in the temperature range 77–350 K in the following computations.

Since analytical solutions of Eq. (8) are very hard to determine and the boundary condition at the detector side possesses a complicated form (as shown below), we resort to a numerical procedure to solve this problem. A finite difference method using an implicit scheme is employed [9]. The thin top plate is in direct contact with the cold tip of the cooler and has a uniform temperature. For this reason, we let a grid at the detector side of the cold well include the top plate of the cold well. This particular grid is called a tip grid hereafter. The following energy balance equation for the tip grid is discretized to be used as a boundary condition in the computation:

$$\rho c \Delta V \frac{\partial T}{\partial t} = -kA_c \left.\frac{\partial T}{\partial x}\right|_{x=L} - h\Delta A_s (T - T_\infty) - (aT + b), \tag{12}$$

where ΔV and ΔA_s are the volume and the surface area of the grid, respectively. We temporarily neglect the thermal capacity of the detector as compared with that of the cold well. However, we evaluate the effects of the thermal capacity of the tip grid in Section 3.2 to simulate the effects of the thermal mass of the detector.

3. Results and discussions

3.1. Steady heat transfer analysis

Fig. 2 shows the steady temperature profile in the cold well for a case where the heat transfer to the cold well surface is present due to the gaseous conduction and the radiation ($h > 0$) as well as for a case in which they are absent ($h = 0$). When $h = 0$, the temperature profile is linear for an obvious reason. On the other hand, when $h > 0$, the surface heat flux causes the temperature profile to bend upward. This makes the temperature gradient at $x = L$ greater than the case where $h = 0$, thereby increasing the heat flux that the cooler should

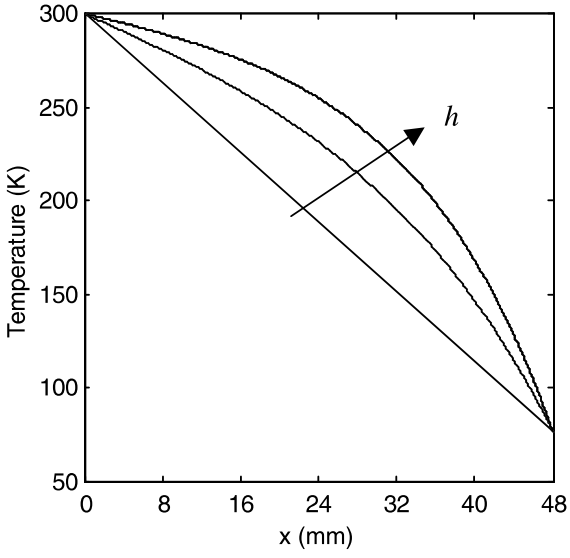

Fig. 2. Steady temperature profile in the cold well. Along the arrow, h increases as $h = 0$, 1.42, and 3. $h = 1.42$ corresponds to a case where the gas pressure is 10^{-2} Torr, and the surface emissivity 0.02.

carry away. This steady cooling load comprises the conductive heat leakage, the heat flux to the surface of the cold well, and the heat generation by the detector array when it is biased. Especially, the effects of the gaseous conduction and the radiation, i.e., the surface heat flux, on the cooling load can be determined by considering the following nondimensional cooling load, Q_L^*:

$$Q_L^* = \frac{Q_L}{-kA_c(T_d - T_\infty)/L}, \tag{13}$$

where Q_{bias} has been set to be 0. Therefore, Q_L^* represents the ratio of the total cooling load including the surface heat flux to the pure bore conduction leakage. From Eq. (3), we obtain

$$Q_L^* = mL\frac{\cosh mL}{\sinh mL}, \tag{14}$$

which reveals that the nondimensional parameter mL determines the relative significance of the surface heat flux to the pure bore conduction. Fig. 3 shows Q_L^* vs. mL, in which mL varies within the parameter range of our current study.

Now we investigate the effects of individual parameters on the cooling load. Fig. 4 summarizes the effects of the gas pressure (a), cold well surface emissivity (b), and the bore conductivity (c). As the gas pressure increases, the cooling load increases in a way similar to h_{gc} (see Appendix A). Especially, when the gas pressure is below $\sim 10^{-3}$ Torr, the gaseous conduction has a negligible effect. However, as the gas pressure increases above $\sim 10^{-3}$ Torr, the gaseous conduction, thus the required cooling load, rapidly increases. As the gas pressure approaches 1 Torr, the cooling load tends to saturate since above 1 Torr, the gas conductivity becomes independent of the gas pressure. As shown in Fig. 4(b), the surface emissivity has insignificant effects on the cooling load when it is below 0.1, where the usual gold film's emissivity ranges (here it is recalled that the cold well surface is gold-plated). However, as the emissivity increases further, its effect is no longer negligible. The reason that the increase rate of the cooling load with the emissivity slows down for high gas pressures is because the effect of h_{rad} on the total h does not increase as dramatically as when the gas pressures (i.e., h_{gc}) are low. The bore conductivity exerts a direct effect on the cooling load as shown in Fig. 4(c). It is interesting to note that while the cooling load linearly increases with the conductivity regardless of the gas pressure for sufficiently high bore conductivity, the cooling loads for high gas pressures increase much faster than those for low pressures do in the range where the conductivity is low. This can be understood by considering the limit form of Eq. (3) when $m \gg 1$, i.e., $h/k \gg 1$ due to very small k. Then we easily obtain $Q_L \propto \sqrt{hk}$ thus the shape of the cooling load curve in a small k region is explained. As the gas pressure increases, the range where $m \gg 1$ holds gets wider, so does the range where the behavior following $Q_L \propto \sqrt{hk}$ is observed. As the bore conductivity increases to overwhelm the effects of h, the heat leakage is dominated by the bore conduction and the cooling load linearly increases with the bore conductivity. We also note that Fig. 4 indicates that when the gas pressure is very low, the steady cooling load of the cryochamber ($k = 0.8$ W/m/K) is approximately 0.1 W. This agrees with the known test data of a cryochamber having similar dimensions as the one currently investigated (GEC-Marconi type 66RPW/T2982) [10].

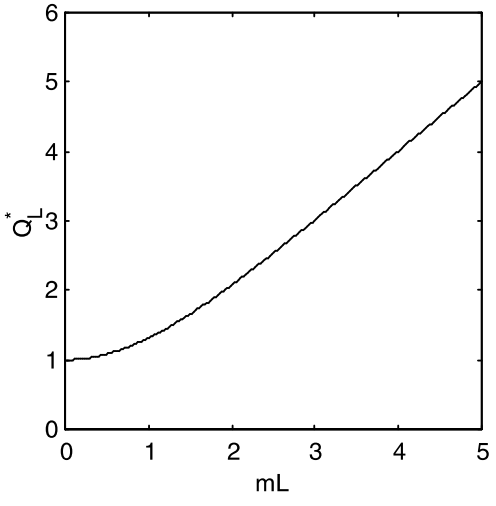

Fig. 3. Nondimensional cooling load Q_L^* vs. mL.

3.2. Transient heat transfer analysis

As discussed above, we employ a numerical method to investigate the transient thermal response of the IR detector cryochamber. Since the refrigeration is provided at one end of a long thin cold well, a steep temperature gradient is initially generated in a region neighboring the cold end. Therefore, we use spatial grids which are denser in the region close to the cold tip than in the remaining part of the cold well.

To check the accuracy of our computational method, a similar problem whose analytical solution is known a priori is solved numerically and the results are compared with the analytical solution. To this end, we consider a semi-infinite body whose surface at $y = 0$ is cooled at a rate $Q_c = aT(t, y = 0) + b$. Here y can be regarded as $y = L - x$ based on the configuration shown in Fig. 1. This case models a thin cold well having a constant cross-section with no surface heat flux. The semi-infinite body assumption is used since the thermal penetration depth is much smaller than the cold well length in the time span of our interest, as will get clear in the following. By letting $\tilde{\theta} = T + b/a$, the governing equation is given by

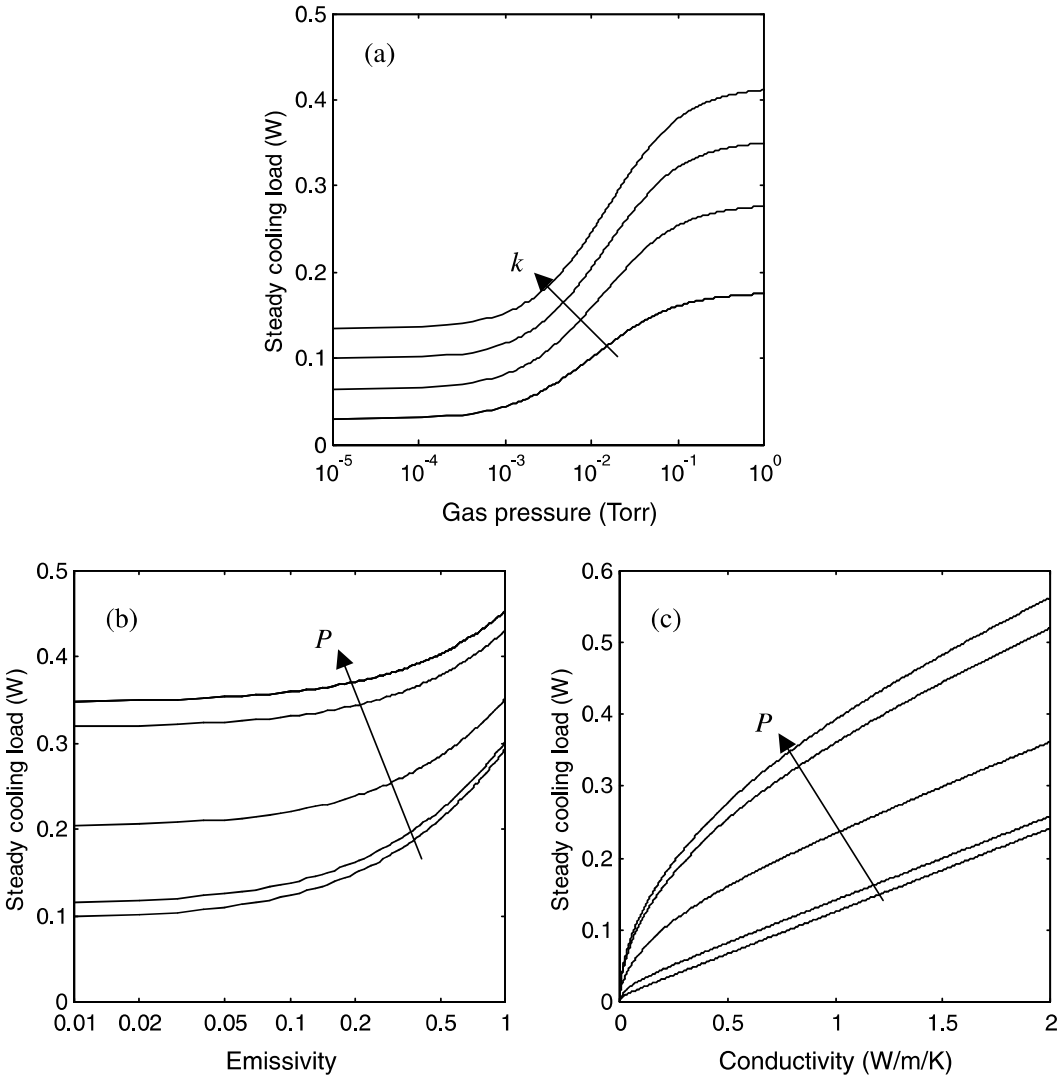

Fig. 4. Effects of the gas pressure (a), the cold well surface emissivity (b), and the bore conductivity (c) on the steady cooling load. In (a), along the arrow, k increases as $k = 0.2,\ 0.5,\ 0.8$, and 1.1 W/m/K. In (b) and (c), along the arrow, P increases as $10^{-4},\ 10^{-3},\ 10^{-2},\ 10^{-1}$, and 1 Torr. In all the cases, Q_{bias} is ignored.

$$\frac{\partial\tilde{\theta}}{\partial t} = \alpha\frac{\partial^2\tilde{\theta}}{\partial y^2}. \tag{15}$$

As the boundary conditions, we have

$$-\frac{\partial\tilde{\theta}}{\partial y} + \tilde{h}\tilde{\theta} = 0 \quad \text{at } y = 0, \tag{16}$$

where $\tilde{h} = a/kA_c$, and

$$\tilde{\theta} \to T_\infty + \frac{b}{a} \quad \text{as } y \to \infty. \tag{17}$$

The initial condition becomes

$$\tilde{\theta} = T_\infty + \frac{b}{a} \quad \text{at } t = 0. \tag{18}$$

Carslaw and Jaeger [11] provides the analytical solution to this problem, and the surface temperature T_s at $y = 0$ is given by

$$T_s = \left(T_\infty + \frac{b}{a}\right)\exp(\tilde{h}^2\alpha t)\,\text{erfc}(\tilde{h}\sqrt{\alpha t}) - \frac{b}{a}. \tag{19}$$

Fig. 5 compares the analytically obtained T_s and the corresponding computational values, proving the accuracy of our computation. Using this computational method, we investigate the effects of various parameters on the transient cooling behavior of the cryochamber.

Fig. 6(a) shows the temperature profile in the cold well evolving with time. For the time span of our interest, in which the detector cools down to 77 K from 300 K, the temperature changes do not penetrate farther than ~15 mm from the cold tip. Fig. 6(b) shows the detector temperature dropping with the time and reaching 77 K after 27.85 s. It should be noted that the temperature decreases rapidly in the early stages due to high refrigeration capacity while the decrease rate is

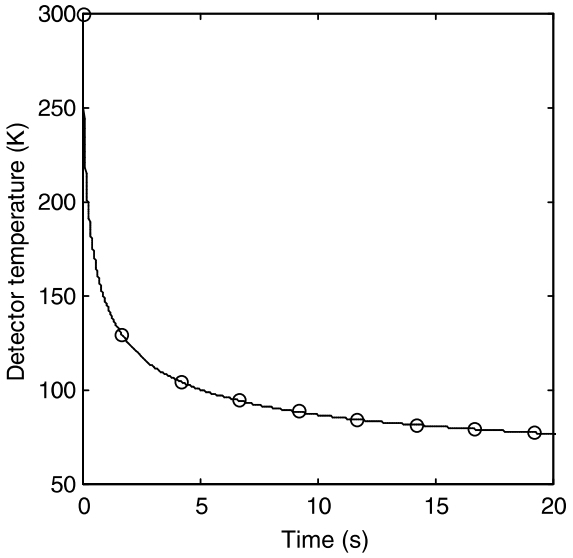

Fig. 5. Verification of computational accuracy. The line is the analytical solution and circles are from the numerical simulation. 500 grids are used between $x = 0$ to $0.98L$, and 1000 grids between $x = 0.98L$ to L.

slowed down when the temperature is low for low refrigeration capacity.

Fig. 7 shows the dependence of the cool-down time on parameters such as gas pressure (a), bore conductivity (b), thermal capacity of the tip grid (c), and ambient temperature (d). Fig. 7(a) reveals that the gas pressure has an insignificant effect on the cool-down time contrary to the steady cases. It is because the area where the gaseous conduction occurs, i.e., where T differs from T_∞, is confined to a narrow region near the cold tip. On the other hand, the entire region participates in the gaseous conduction in the case of the steady state. The thermal penetration depth, δ_T, can be scaled as $\delta_T \sim \sqrt{\alpha t}$, and it does not grow much until the detector temperature reaches 77 K, as shown in Fig. 6(a). As a matter of fact, it takes about 600 s for δ_T to grow to L. The apparent increase in the cool-down time for high k, albeit weak, is thus attributed to the increase of α and consequently large δ_T. Fig. 7(b) shows that the bore conductivity has a significant influence as in the steady cases (Fig. 4(c)). The increase of the difference between high and low gas pressure cases can be explained by the aforementioned increase in δ_T. Fig. 7(c) shows the effect of the thermal capacity of the tip grid or the detector assembly's thermal mass. As the thermal capacity increases, the cool-down time increases almost linearly. However, it should be noted that doubling the thermal capacity does not necessarily cause the cool-down time to double as well. It is because the cooler needs to refrigerate the cold well region within the penetration depth as well as the tip grid or the detector. Therefore, the effective thermal mass that should be cooled is to be regarded as the sum of those of the detector and a portion of the cold well within the

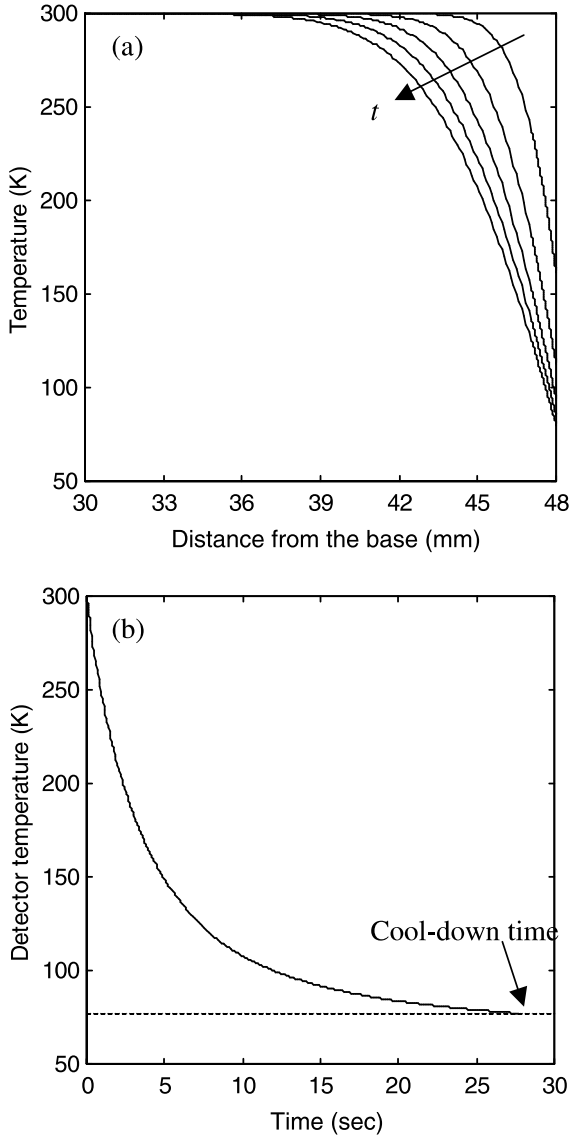

Fig. 6. Transient temperature profile in the cold well (a), and the response of the detector temperature with time (b). In (a), along the arrow, the time increases as $t = 4.15,\ 9.15,\ 14.15,\ 19.15$, and 24.15 s. The horizontal line in (b) indicates 77 K. The gas pressure $P = 10^{-4}$ Torr is assumed in the computation.

penetration depth. Fig. 7(d) simulates the effects of the ambient temperature changes on the cool-down time. It is remarkable that the cool-down time increases more steeply as the ambient temperature increases. This can be understood by scaling the refrigeration capacity Q_c, when the detector temperature reaches 77 K, as

$$Q_c \sim kA_c \frac{\Delta T}{\sqrt{\alpha t_c}}, \tag{20}$$

where ΔT is the difference between the detector temperature and the ambient temperature, and t_c denotes the cool-down time. Using Eq. (20), one can easily show that

$$t_c \propto k(\rho c)\Delta T^2 \tag{21}$$

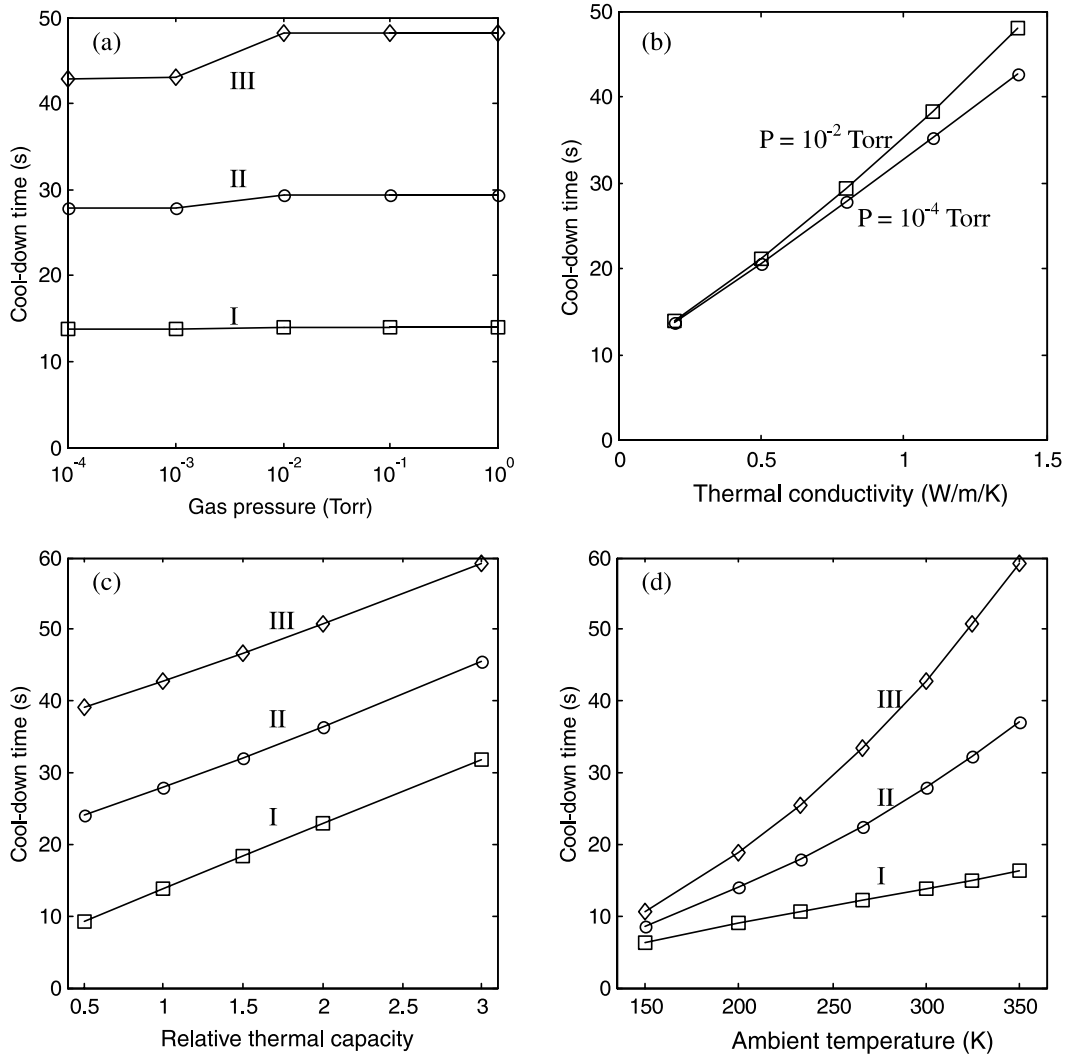

Fig. 7. Dependence of the cool-down time on the gas pressure (a), the bore conductivity (b), the thermal capacity of the tip grid (c), and the ambient temperature (d). In (a), (c), and (d), curves I, II, and III correspond to when $k = 0.2,\ 0.8$, and 1.4 W/m/K, respectively. In (c), the relative thermal capacity = 1 corresponds to a normal case where the top plate of thickness 1 mm is included in the tip grid. The relative thermal capacity = 2, for example, means that the tip grid's thermal capacity is double the normal tip grid's thermal capacity.

for constant A_c and Q_c. This relationship suggests that the cool-down time increase with ΔT^2, explaining the aforementioned steep increase of the cool-down time at high ambient temperatures. In addition, the linear dependence of t_c on the bore conductivity (Fig. 7(b)) and on the thermal capacity (Fig. 7(c)) can also be deduced from this relationship.

4. Concluding remarks

This work investigates the cooling characteristics of an IR detector cryochamber based on a typical configuration. It is shown that the heat leakage from the warm environment to the cold detector consists of the conduction through the cold well, the gaseous conduction, and the radiative heat transfer. Both the steady and transient cooling performances are modeled and their dependence on various parameters, such as the bore conductivity, gas pressure, cold well surface emissivity, and ambient temperature is examined. In the modeling, the conductive heat transfer in the cold well is assumed to be one-dimensional due to its small thickness. The thermal conductance of gaseous conduction depending on the gas pressure is obtained using the theory of rarefied gas heat transfer. In the steady heat transfer analysis, we compute the steady cooling load required to maintain the detector at its nominal operating temperature 77 K. In doing so, the cold well is modeled as a fin subjected to the surface heat flux due to gaseous conduction and radiation. For the transient heat transfer analysis, a numerical method is employed. The rate of heat subtracted by the cooler at the cold tip is modeled to be linear with the tip temperature.

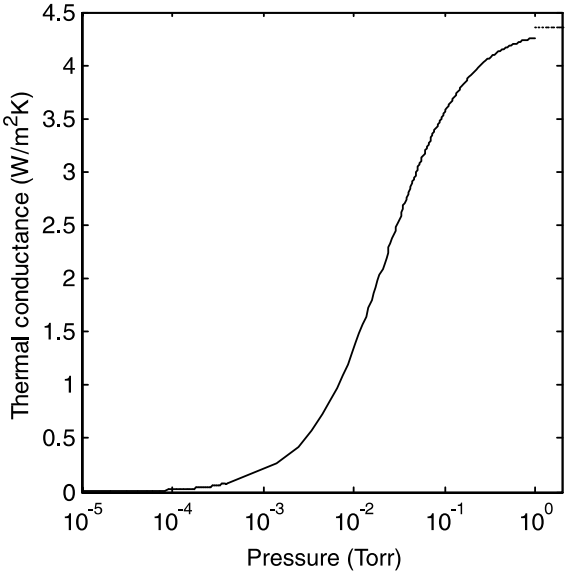

Fig. 8. The thermal conductance of the gaseous conduction depending on the gas pressure. At $P = 1$ Torr, two curves do not connect smoothly revealing the limit of the interpolation formula, but its effect is not significant enough to affect our computation results.

We conclude with comparing the parametric dependence of the steady cooling performance and that of the transient cooling performance. (1) The gaseous conduction plays an important role in determining the steady cooling load, whereas the cool-down time is negligibly affected due to a short thermal penetration depth. It should be, however, noted that if a system has sufficiently long penetration depth due to high thermal diffusivity of the cold well, the gaseous conduction becomes important in determining the cool-down time as well. (2) The steady cooling load increases linearly with the bore conductivity when it is high, but when the gas pressure is high and the bore conductivity is low, $Q_L \propto \sqrt{hk}$. On the other hand, the cool-down time increases almost linearly with k for an entire parametric space. (3) The steady cooling load increases linearly with ΔT as is evident from Eq. (3). However, the cool-down time is rather proportional to ΔT^2.

Acknowledgements

The authors are grateful to Ministry of Science and Technology (MOST) and Agency for Defense Development (ADD), Korea for the support of this work through the Dual Use Technology Program.

Appendix A. Rarefied gas conduction

Since the gas pressure of our interest is very low ($\sim 10^{-5}$ to ~ 1 Torr), the molecular mean free path λ is not negligibly small compared to a characteristic dimension (in our case, the gap spacing) l_s. This requires the consideration of heat transfer in a rarefied gas, whose fundamental theory is well established [12,13]. In the following, we obtain the thermal conductance of gaseous conduction corresponding to the configuration we study.

The Knudsen number, Kn, defined as

$$\mathrm{Kn} = \frac{\lambda}{l_s}, \tag{A.1}$$

describes the degree of rarefaction and determines the heat transfer regimes as follows; free molecule ($\mathrm{Kn} > 10$), transition ($10 > \mathrm{Kn} > 0.1$), temperature jump or slip ($0.1 > \mathrm{Kn} > 0.01$), and continuum ($\mathrm{Kn} < 0.01$). Knudsen's formula for free molecule conduction gives the heat flow, Q_{fm}, between two concentric cylinder surfaces at temperatures T_i and T_o, and at radii r_i and r_o [13]:

$$Q_{fm} = 2\pi r_i L \left[\frac{1}{\tilde{\alpha}_i} + \left(\frac{r_i}{r_o}\right)\left(\frac{1}{\tilde{\alpha}_o} - 1\right)\right]^{-1} \times \frac{P(C_v + \hat{R}/2)}{(2\pi \hat{M}\hat{R}T_g)^{1/2}}(T_i - T_o), \tag{A.2}$$

where L is the length of cold well, $\tilde{\alpha}_i$ and $\tilde{\alpha}_o$ are the accommodation coefficients of the inner and outer surfaces, respectively, P is the pressure, C_v the molar heat capacity at constant volume, $\hat{R}$ the molar gas constant, $\hat{M}$ the molecular weight of the gas, and T_g the gas temperature. The accommodation coefficient, $\tilde{\alpha}$, is defined as

$$\tilde{\alpha} = \frac{E_i - E_r}{E_i - E_w}, \tag{A.3}$$

where E_i and E_r are the incident and reflected energies of a gaseous molecule from the surface, and E_w is the energy that the molecule should have carried if it had completely accommodated its energy to the wall temperature [12]. The value of the accommodation coefficient depends on the composition and temperature of the gas and the surface. However, it is experimentally known that the accommodation coefficients of air are close to unity except on surfaces that have had unusual preparation [8,13]. Hence we assume $\tilde{\alpha}_i = \tilde{\alpha}_o = 1$ here. For transition and slip regimes, the following interpolation formula is used [13]:

$$\frac{Q_t}{Q_{fm}} = \left[1 + \left(\frac{Q_{fm}}{Q_c}\right)\right]^{-1}, \tag{A.4}$$

where Q_t and Q_c denote the heat flux in the transition/slip regime and the continuum heat flux, respectively. The continuum heat flux, Q_c, between concentric cylinder surfaces is given by

$$Q_c = \frac{2\pi L}{\ln(r_o/r_i)} k_{air}(T_i - T_o), \tag{A.5}$$

where k_{air} is the thermal conductivity of air as a continuum.

Since the heat transfer regimes above are divided according to the Knudsen number, now we convert the criteria to those using the gas pressure which are more practical. The molecular mean free path λ is given by [14]

$$\lambda = \frac{1}{\sqrt{2}\pi d^2 n}, \tag{A.6}$$

where d is the molecular diameter of air and $d \approx 0.37$ nm. The number of molecules per unit volume, n, can be written as follows, for a perfect gas:

$$n = \frac{P}{k_B T}, \tag{A.7}$$

where k_B is the Boltzmann constant ($k_B = 1.38054 \times 10^{-23}$ J/K). Therefore, the free molecule conduction arises when $P < P_{fm}$:

$$P_{fm} = \frac{k_B T_g}{10\sqrt{2}\pi d^2 l_s}, \tag{A.8}$$

which is given by $P_{fm} = 4 \times 10^{-4}$ Torr when T_g is assumed to be the average temperature of the maximum (300 K) and minimum (77 K) temperature in the chamber. It is suggested that the continuum properties of gases can be used for pressures down to about 1 Torr [6]. Therefore, the thermal conductance of a continuum air between concentric cylinders is given by

$$h_{gc} = \frac{k_{air}}{r_i \ln(r_o/r_i)}. \tag{A.9}$$

From Eq. (A.4), we obtain the following regimes of thermal conductance of the gaseous conduction, h_{gc} (W/m^2 K), depending on gas pressure (Pa):

$$h_{gc} = 1.48P \quad \text{for } P < P_{fm}, \tag{A.10}$$

$$h_{gc} = \frac{1.48P}{1 + 0.34P} \quad \text{for } P_{fm} < P < 1 \text{ Torr}, \tag{A.11}$$

$$h_{gc} = 4.35 \quad \text{for } P > 1 \text{ Torr}. \tag{A.12}$$

Fig. 8 shows h_{gc} vs. P.

References

[1] Morten FD. Applications of infrared detectors. In: Infrared detectors and their applications. Eindhoven, Netherlands: Philips Publication Dept.; 1971 [Chapter 1].
[2] Kaplan H. Practical applications of infrared thermal sensing and imaging equipment. Bellingham (WA): SPIE; 1992.
[3] Fischer RE. Lens design for the infrared. In: Hartmann R, Smith WJ, editors. Infrared optical design and fabrication. Bellingham (WA): SPIE; 1991.
[4] Walker G. Cryocoolers, part 1: fundamentals. New York: Plenum Press; 1983.
[5] Walker G. Cryocoolers, part 2: applications. New York: Plenum Press; 1983.
[6] Mills AF. Heat transfer. Concord (MA): Irwin; 1992.
[7] Arpaci VS. Conduction heat transfer. Abridged ed. Needam Heights, MA: Ginn Press; 1991.
[8] Flynn TM. Cryogenic engineering. New York: Marcel-Dekker; 1997.
[9] Patankar SV. Numerical heat transfer and fluid flow. Washington: McGraw-Hill; 1980.
[10] Kim NH. Private communication.
[11] Carslaw HS, Jaeger JC. Conduction of heat in solids, 2nd ed. Oxford (UK): Oxford University Press; 1959.
[12] Devienne FM. Low density heat transfer. Adv Heat Transfer 1965;2:271–356.
[13] Springer GS. Heat transfer in rarefied gases. Adv Heat Transfer 1970;7:163–218.
[14] Vincenti WG, Kruger Jr CH. Introduction to physical gas dynamics. New York: Wiley; 1965.